Review

A Study on Graphene—Metal Contact

Wenjun Liu [1], Jun Wei [2], Xiaowei Sun [3,4] and Hongyu Yu [3,*]

[1] Department of Materials Engineering, The University of Tokyo, 7-3-1, Hongo, Bunkyo,
 Tokyo 113-8656, Japan; E-Mail: liu@adam.t.u-tokyo.ac.jp

[2] Singapore Institute of Manufacturing Technology, 71 Nanyang Drive, Singapore 638075;
 E-Mail: jwei@simtech.a-star.edu.sg

[3] Department of Electronic and Computer Engineering, South University of Science and Technology,
 Shenzhen, Guangdong 518055, China; E-Mail: exwsun@ntu.edu.sg

[4] Division of Microelectronics, School of Electrical and Electronic Engineering, Nanyang
 Technological University, 639798 Singapore, Singapore

* Author to whom correspondence should be addressed; E-Mail: yu.hy@sustc.edu.cn;
 Tel.: +86-755-8624-5722.

Abstract: The contact resistance between graphene and metal electrodes is crucial for the achievement of high-performance graphene devices. In this study, we review our recent study on the graphene–metal contact characteristics from the following viewpoints: (1) metal preparation method; (2) asymmetric conductance; (3) annealing effect; (4) interfaces impact.

Keywords: graphene; field-effect transistor; contact resistance; Raman

1. Introduction

Graphene is a single atomic sheet of carbon atoms in a honeycomb lattice, where the carbon-carbon bonds in the plane are sp^2 hybridized. Ever since it was firstly isolated from micromechanical cleavage of bulky graphite flakes in 2004 [1], graphene has been widely investigated owing to its unique and attractive electrical, physical and chemical properties [1–11]. Graphene is an energy gapless material, in which the conduction and valence bands meet at the Dirac point. Its linear electronic dispersion relation results in a zero effective mass of the carrier with a high Fermi velocity. This material thus exhibits an extraordinarily high carrier mobility of more than 200,000 cm^2 $V^{-1}s^{-1}$ [12].

It is considered to be a potential channel material for field-effect transistors (FETs) application. In addition, graphene has been applied to various practical device applications, such as high frequency devices [9], gas sensors [5,13], flexible electronics [14,15], and photonics [16,17]. In spite of the very high mobility in the graphene channel, however, the contact resistance between graphene and metal electrodes is crucial to achieving a high performance from the graphene [18–20], especially the high on-state current. It has been reported that the control of contact properties is more important than the intrinsic channel mobility, as otherwise the merit of high mobility from the graphene will be diminished significantly [18]. In this paper, we provide a study on the characteristics of graphene–metal contact from the perspectives of: (1) metal preparation method; (2) asymmetric conductance; (3) annealing effect; and (4) interface impact. These findings offer insightful information to achieve high performance graphene devices via process optimization.

2. Impact of Metal Preparation

When measuring contact resistance, the contribution from the graphene sheet resistance should be minimized or eliminated. There are several methodologies to extract the graphene–metal contact resistance, including the transfer length [21,22], four-probe/two-probe [18,19,23], and residual resistance methods [20,24]. We use the last two methods to extract the contact resistance. Ti has been used as metal electrodes in carbon-based devices because of its excellent adhesive capability in SiO_2 substrate or other insulators [25]. In this section, we take Ti/graphene as an example to study the impact of different metal deposition methods on R_c.

The total resistance between two contacts is the sum of the semiconductor resistance, the contact resistance, and the metal resistance, where the metal resistance can be neglected owing to good control of metal electrode growth. By subtracting the graphene resistance from the total resistance, one obtains the total contact resistance. The contact resistance for each contact is thus obtained as half of the total resistance [18,26,27]:

$$R_c = \frac{1}{2}(R_{total} - R_g)$$

(1)

where R_c is the contact resistance between graphene and metal, which is assumed to the identical for the two contacts in back-gate graphene FETs; R_{total} is the total resistance measured between source and drain; R_g is the graphene resistance in channel, derived by $R_g = (V_2 - V_3)/I$, schematically shown in inset in Figure 1b.

Figure 1a shows the $I - V$ characteristics of SLG (single-layer graphene)/Ti devices, where Ti is grown by electron-beam evaporation (EBM) and sputter processes, respectively. In our experiments, graphene is produced by mechanical exfoliation from bulk graphite. Subsequently, graphene is transferred onto degenerated silicon substrate with a thermally grown 90 nm SiO_2, serving as a conventional back-gate dielectric. R_{total} can be extracted from the linear $I - V$ curves. The optical image of measured device is shown in inset in Figure 1(a). The linear $I - V$ characteristic indicates that the Ti/SLG contact is ohmic. Note that there are also ohmic contacts between graphene and other metals in our samples, e.g., Al, Ag, Pd, Ni, Au. However, there is a Schottky junction between graphene nano-ribbon (GNR) and metals [28]. The nonlinear $I - V$ characteristic has been reported in GNR–Au, GNR–Al contacts theoretically and experimentally [29]. This Schottky effect in GNR–metal contacts

stems from the creation of energy band gap in GNR, where the energy band gap increases with reduction of the GRN width [8]. The graphene resistance R_g is measured at the force current from 1 μA to 1 mA, shown in Figure 1b. It was found that R_g is almost the same at different force currents. By combining the results from two-probe (Figure 1a) and four-probe measurement (Figure 1b), R_c is quantitatively addressed. The R_c of EBM sample is observed to have a lower R_c of 0.83 $k\Omega$ as compared to sputter one of 4.2 kΩ. Note that the poor on/off ratio is observed in our graphene FETs, owing to its gapless characteristic.

Figure 1. (**a**) The $I_{2p} - V_{2p}$ plots of Ti/SLG devices at for EBM and sputter processes, respectively. The optical image of measured device is shown in inset of Figure 1a; (**b**) The graphene resistance R_g (R_{4p}) between two probes as a function of force current. The schematic for four-probe measurement is shown in inset of Figure 1b. R_c can thus be quantitatively obtained by combining the results from two-probe and four-probe measurements. Reprinted with permission from [27]. Copyright (2011) by the Electrochemical Society.
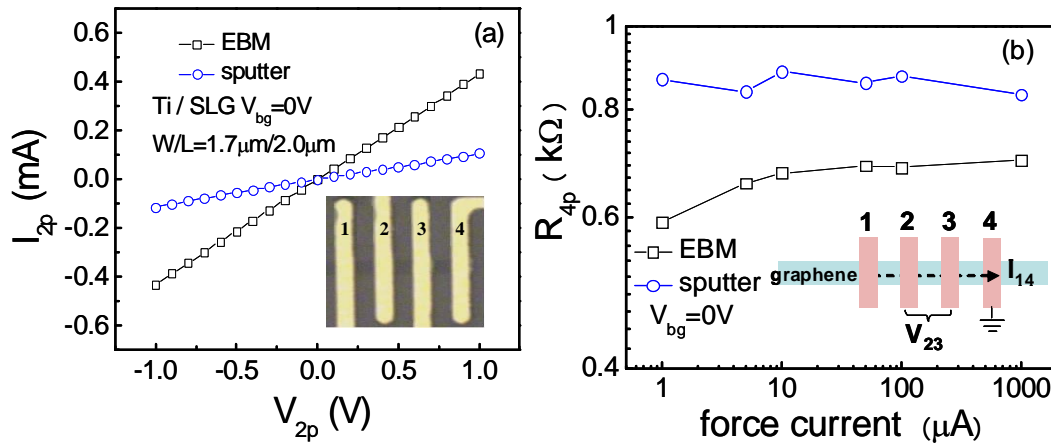

Note that in the four-probe measurement, the back-gate electrode of graphene FETs is floating, and R_g is almost a constant. While in residual resistance measurement, the R_g is changeable according to the modulation of carrier density in graphene channel. The R_c then can be determined as follows [20]:

$$R_c = \frac{1}{2}(R_{total}(V_{bg}) - R_{g}(V_{bg}))$$ (2)

where V_{bg} is back-gate voltage; R_g is V_{bg} dependent, owing to the modification of carrier density in graphene channel; The residual resistance R_{resi}, which is the saturated resistance at high V_{bg}, is equal to $2R_c$ due to negligible R_g at large negative V_{bg}, indicating the total resistance is mainly from the contribution of contact resistance [20], schematically illustrated in Figure 2a,b. Using residual resistance measurement method, one may obtain that R_c is 0.78 $k\Omega$ and 4.1 $k\Omega$ for EBM and sputter Ti/SLG devices, respectively, as shown in Figure 3. It was found that R_c extracted from the two-probe/four-probe and residual resistance measurement methods is in excellent agreement with each other. The $I_{ds} - V_{ds}$ characteristics at various back-gate voltages also exhibit the linear behavior, shown in the inset in Figure 2.

Figure 2. (**a**) The schematic of residual resistance measurement; (**b**) The equivalent circuit for graphene FETs. R_g can be modulated by back-gate voltage; (**c**) $R - V_{bg}$ plots of the Ti/SLG device prepared by EBM and sputter processes, respectively. The residual resistance R_{resi} equals to $2R_c$ at high negative voltage. The $I_{ds} - V_{ds}$ plots as a function of V_{bg} are shown in the inset in Figure 2. R_c is larger for the sputtered Ti/SLG device than EBM one.
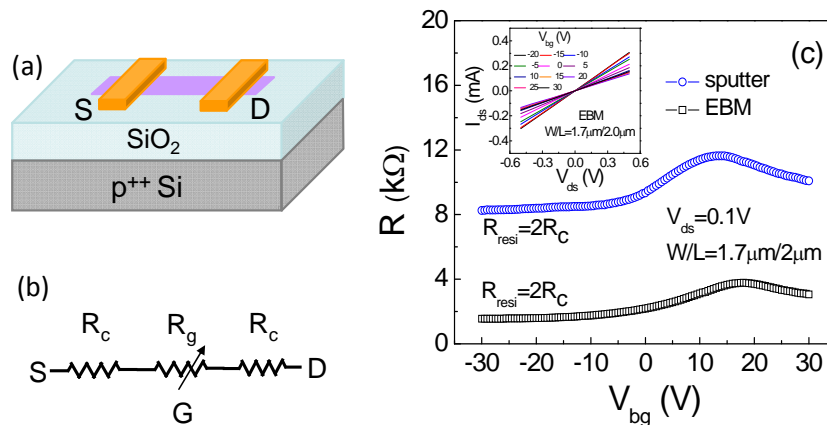
The measured contact resistivity ρ_c of SLG, DLG (double-layer graphene), MLG (multi-layer graphene)/Ti devices, prepared by EBM and sputter processes, is summarized in Figure 3. The standard error is calculated from eight samples for each group. For all the devices fabricated by the EBM process, the ρ_c does not exhibit strong dependence on the number of graphene layers. It is consistent with the early work, where R_c of SLG, DLG, and TLG FETs (also EBM samples) is insensitive to layer thickness [30], while for the devices prepared by sputter process, the ρ_c exhibits layer dependence and increases with decreasing the number of layers. It is worth noting that the ρ_c of Ti/SLG and Ti/DLG from the former is significantly smaller than that from latter. Note that there is a negligible difference in ρ_c between the EBM and sputter samples. Thus it is proposed that the sputter Ti atoms would only effectively affect the top layers (up to two layers) of graphene in our case. It is believed that, for MLG, after the top layers create the vacancies, the metal can "penetrate" through the vacancies to contact with the bottom layer directly. Figure 4 shows the ρ_c distribution of Ti/SLG devices prepared by sputter processes at various powers. It is also observed that the ρ_c increases more than two orders of magnitude as sputter power enhances. It was reported that the ρ_c can reach $10^9 \, \Omega \, \mu m$ in case of sputtered Ti on SLG or MLG [18]. It infers more carbon atoms are milled away when the sputter power increases.

Figure 3. The distribution of ρ_c of Ti/SLG, DLG, MLG devices prepared by EBM and sputter processes, respectively. The solid symbols represent the average ρ_c and the error bars come from standard error. The average ρ_c of sputtered Ti/SLG and DLG devices is larger than EBM ones. Furthermore, the ρ_c of the SLG device is larger than that of the DLG (MLG) devices for the sputter process. Reprinted with permission from [27]. Copyright (2011) by the Electrochemical Society.
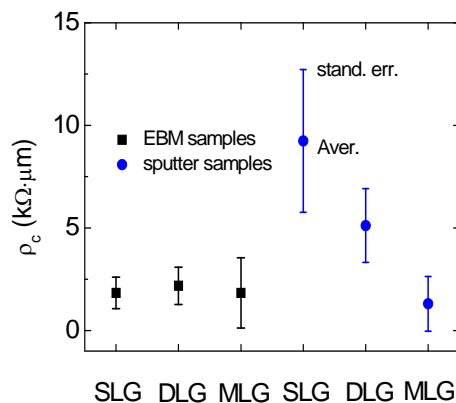

Figure 4. The distribution of the ρ_c of Ti/SLG devices prepared by sputter processes at different powers (power 1 < power 2). The ρ_c increases more than two orders of magnitude when the sputtering power increases.
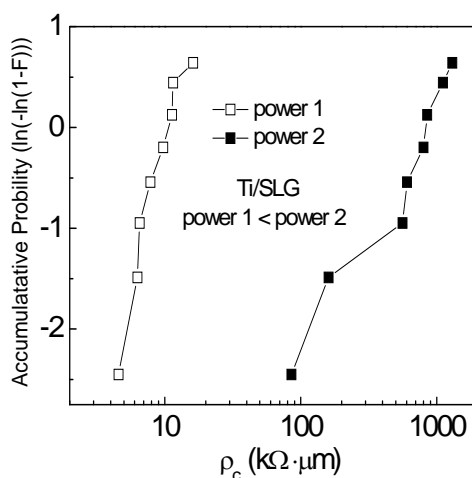

Figure 5 shows the Raman spectra of SLG, DLG, TLG (triple-layer graphene) with and without metal deposition, where they are prepared by (a) EBM; and (b) sputter processes, respectively. Raman spectroscopy has been used to physically probe the electronic structure of graphite and graphene without damaging the sample [31–34]. Since our graphene sheet is prepared by mechanical exfoliation from bulky graphite, there is no D band in Raman spectra of graphene before metal deposition. There are only two main characteristic peaks of G and 2D bands before metal growth, where the peak position for G and 2D bands are around 1580 and 2670 cm^{-1}, respectively. For EBM samples, there is negligible D band, around at 1350 cm^{-1}, after Ti deposition by EBM process. It is worth noting that D bands are formed after receiving sputtered Ti for all SLG/DLG/TLG samples, significantly different from the ones after EBM process. The D band is caused by disordered or defected structure of

graphene sheet [31,35,36]. The intensity ratio of D band to G band (I_D/I_G) is usually used to estimate the amount of defects in carbon materials. Accordingly, compared to sputtered Ti/graphene contact, a Ti/graphene contact prepared by EBM corresponds to very low defects or carbon vacancies in graphene. It has been reported that the formation energy of carbon vacancies in graphite is around 7.4 eV [37,38]. Thus, the ion energy in the sputter process should be larger than that to create the carbon vacancies in graphene. Generally, it is believed that sputtered Ti atoms possess larger kinetic energy compared to the EBM case, and the energy could be transferred to the graphene layer, resulting in the removal of carbon atoms from the graphene lattice and creating of the carbon vacancies.

Figure 5. Raman spectra of 1–3 layers graphene with and without Ti (~9 nm) deposition by (**a**) EBM; and (**b**) sputter process, respectively. The noticeable D band in sputtered Ti/grapheme junction, which is related to the defects (carbon vacancies) in graphene, is marked by a red dash box in Figure 5b; (**c**) The optical image of Raman sample. 1, 2, 3, and 4 in Figure 5c represent SLG, DLG, TLG, and MLG (multi-layer graphene), respectively. Reprinted with permission from [27]. Copyright (2011) by the Electrochemical Society.
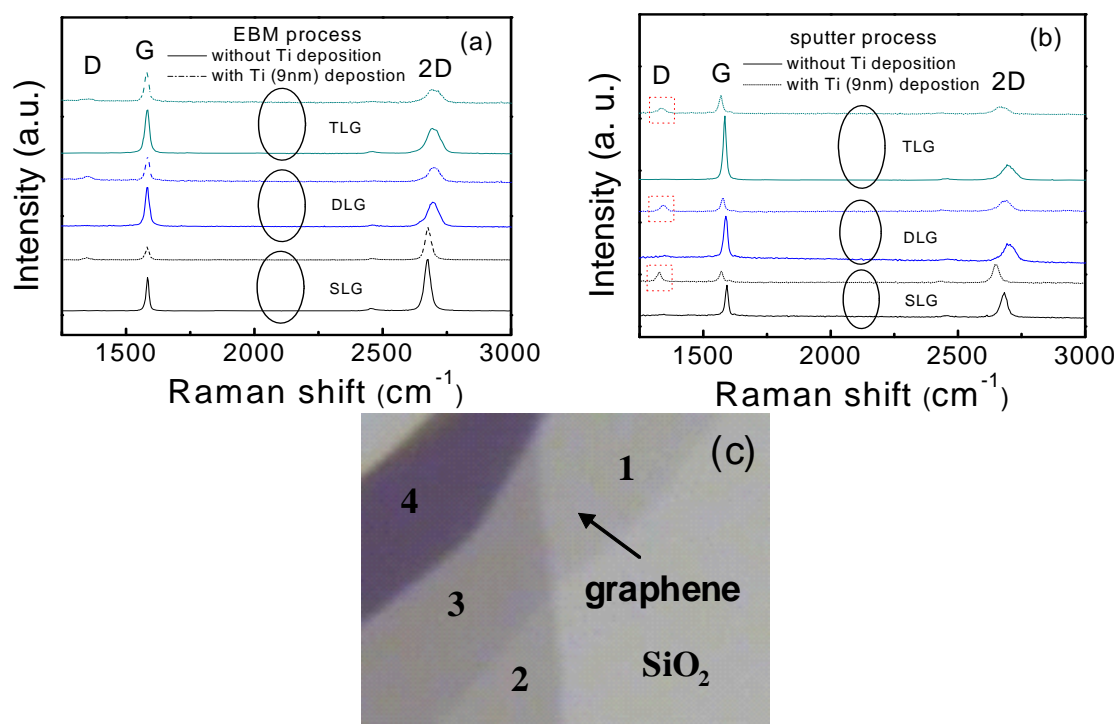

In addition to the presence of the D band, the G and 2D band shifts are also observed in sputtered SLG, DLG, and MLG/Ti contacts. In the meantime, it is found that there is no noticeable band shift after Ti deposition onto graphene, where Ti is grown by EBM process, indicating no change in lattice constant in graphene and graphite, shown in Figure 5a. On the contrary, the 2D band and G band have an obvious red shift of ~30 cm^{-1} and ~20 cm^{-1} after Ti deposition by sputter process. G band shift caused by charge doping through phonon-electron coupling has been reported by Yan *et al.* [39]. The 2D band is a second-order two-phonon process and exhibits a strong frequency dependence on the excitation laser energy [32]. However, the additional band shift will be narrow at ~10 cm^{-1} in case of

charge doping [39,40]. Therefore, this band shift cannot be attributed only to the charge doping effect. Tensile stress is also reported to cause the red shift in graphene; the red shift expands with increasing tensile stress [41,42]. As the 2D band originates from the two-phonon double-resonance process, it is closely related to the band structure of graphene layers. It is thus believed that the sputter process can lead to tensile strain in graphene underneath Ti owing to defects formation, thereby enlarging the lattice constant of graphene. The red shift of the 2D and G bands can thus be understood as the tensile strain weakening the bond and thus lowering the vibration frequency due to the elongation of C-C bonds [42].

A schematic model has been proposed to explain the difference in graphene–metal contacts between large and small grains in contact metal [22]. In their model, the large grains and rough surface of contact metal play an important role in the contact area and small contact area results in large contact resistance. Then, contact resistance can be affected by the grain size and the uniformity of the contact metal films. For sputtered SLG and DLG/Ti devices, there is also the possibility of a smaller contact area, as parts of carbon atoms are milled away from the pristine graphene structure, accordingly increasing the contact resistance. It must be pointed out that the defected carbon or carbon vacancies not only occur in the graphene underneath the metal, but also at the adjunct region of graphene channel and graphene–metal contact. It was reported that the defected graphene will break the symmetry of regular hexagonal C-C bond structures, thus resulting in the intervalley electron scattering [43,44]; accordingly, the mobility will degrade compared to the pristine one. Note that there is possible carbide formation after Ti deposition onto the graphene, similar to surface-carbide formation in additional Ni deposition on graphene [45]. However, the number of Ti-C bonds is very low and their influence on electron transport is negligible [46]. It was also observed that the significant increase in D band sputtered Al/SLG, Al/DLG contacts, asshown in Figure 6. The I_D/I_G is larger than 2. The 2D band even disappears as the sample is subjected to high sputter power, indicating that the pristine structure of graphene has been significantly destroyed. Note that the reduced R_c is observed in high vacuum deposition condition, suggesting deposition pressure also has a significant influence on the quality of R_c [30].

Figure 6. The Raman spectra of SLG, DLG before and after sputtered Al. The optical image of measured Al/SLG, Al/DLG contacts is presented in the inset.
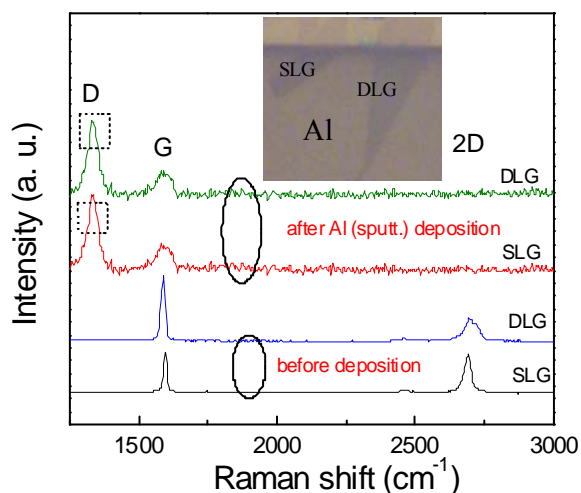
3. Asymmetry Conductance

Because graphene is an energy gapless material, it is very similar to the metal–metal contact when graphene is brought into contact with metal. With metal–metal contact, a small redistribution of electrons can screen the potential difference due to the large carrier density, where the potential difference originates from the work function difference in two metals. The screening length λ is expressed by $1/\sqrt{4\pi N(E_F)}$ [47], where $N(E_F)$ is the DOS at the E_F in graphene. The λ is less than 1 nm for metal–metal contact. However, for graphene–metal contact, DOS is very small compared to metal, especially at the Dirac point, and λ is much larger than that of metal. In addition, graphene itself is sensitive to external perturbations owing to its all-surface and zero volume nature [48]. Charge transfer between graphene and metal may dope the underlying graphene into n-type or p-type, depending on work function differences. Therefore, the metal doping effect must be considered in transfer characteristics of graphene FETs. In Figure 2, it is shown that p-type and n-type branches show a moderate asymmetry and the conductance in the n-type branch is always smaller than that in the p branch. It is consistent with the previous report [18]. This asymmetric conductance behavior was first investigated by comparing devices with invasive electrodes crossing the whole graphene channel width and external electrodes connected to the side of the graphene channel [23]. The graphene FETs with invasive electrode show the asymmetry of conductance in n-type and p-type branches; however, the asymmetry almost never occurs in devices with external electrodes [18,23]. Giovannetti and Khomyakov *et al.* [49,50] applied density functional theory (DFT) to study how graphene is doped by various metals, including Al, Ag, Cu, Au, Pt. The calculated Fermi energy shift (ΔE_F) with respect to the conical point can increase by decreasing the distance between graphene and metal. Xia *et al.*, by using scanning photocurrent microscopy (SPCM), illustrated that the charge doping occurs not only underneath the metal, but also extends hundreds of nanometers into adjacent regions in the graphene channel [51,52]. They separated a graphene FET into three segments: (1) the metal-controlled graphene; (2) the transition region affected by both the metal and the back-gate; and (3) the bulk graphene region controlled only by the back-gate. With the modulation of back-gate voltage, the width of transition region (segment 2) is accordingly modified. In their experiments, the detected photocurrent comes from the p–n junction in the graphene sheet, since the photocurrent is proportional to the potential gradient at the excitation position. It exhibits the different polarities along the graphene channel. Lee *et al.* [53] observed the photocurrent in graphene FETs with the help of SPCM, resulting from p–n junction formation in the graphene sheet. It was also reported that chemical doping can introduce conductance asymmetry. It is caused by a combination of the neutrality point misalignment at the electrode–channel interface and the non-constant DOS of the graphene electrodes [54].

Previously, we implemented scanning Kelvin probe microscopy (SKPM) to experimentally address the work function difference between graphene channel and metal electrodes [55]. The graphene underneath the metal is assumed to be pinned, and the constant potential $\Delta\phi$ can be described as follows [52]:

$$\Delta\phi = \hbar v_F \sqrt{\pi\alpha \left| V_{bg}^{flat} - V_{Dirac} \right|} \tag{3}$$

where $\hbar$ is the Plank constant divided by 2π; V_{bg}^{flat} is the flat band voltage; v_F is Fermi velocity of 0.8×10^6 m/s; α is $2.24 \times 10^{11} cm^{-2} v^{-1}$, which is estimated from a simple capacitor model [56]. The results show that the effective constant potential $\Delta\phi$ for Ti/SLG, Al/SLG, Ag/SLG Pd/SLG is 0.1 eV, -0.22 eV, 0.08 eV, 0.45 eV, respectively. For Ti/SLG, our calculated $\Delta\phi$ is consistent with Xia's report of ~0.12 eV [51] or 0.1 eV [52], Figure 7a–c shows the $R_{total} - V_{bg}$ plots of graphene FETs with different metal electrodes Ag, Pd, Al, respectively. They exhibit an asymmetric behavior in hole and electron transportation branches, including the graphene FETs with Ti electrode, shown in Figure 2. The numerical simulation has shown that the Fermi level of graphene underneath the metal is shifted and may result in asymmetric transfer characteristics [57], which is similar to the aforementioned. The odd resistance is used to characterize the asymmetry in graphene FETs with various metal electrodes. The R_{odd} is defined as follows [23,52]:

$$R_{odd} = \frac{R(\Delta V_{bg}) - R(-\Delta V_{bg})}{2} \tag{4}$$

where $\Delta V_{bg} = V_{bg} - V_{Dirac}$; The R_{odd} is positive for Ti, Ag, Au, Pd, and negative for a Al/SLG FET, indicating hole branch dominating transportation for the Ti, Ag, Au, Pd cases, while electron branch dominates the transportation for Al. It is observed that the Dirac point of measured graphene locates at the region of positive voltage, indicating that our fabrication process introduces a p-type doping in the graphene channel. For Ag (Ti, Au, Pd)/SLG FETs, the p–p–p (p–n–p) junction forms when $V_{bg} < V_{Dirac}$ ($V_{bg} > V_{Dirac}$). While for Al/SLG FETs, the n–p–n (n–n–n) junction forms when $V_{bg} < V_{Dirac}$ ($V_{bg} > V_{Dirac}$). The excess resistance in the electron transportation region for Ag (Ti, Au, Pd)/SLG FETs is the result of the p–n–p junction formation, whereas the n–p–n junction is believed to be the cause of high resistance in the hole transportation region for Al/SLG FETs.

Figure 7. $R_{odd} - V_{bg}$ plots of SLG FETs with various metal electrodes (**a**) Ag; (**b**) Pd; (**c**) Al, respectively. Insets show the Fermi level (red dash) with respect to the Dirac point at the hole and electron transportation regions; (**d**) R_{odd} *vs.* ($V_{bg} - V_{Dirac}$) plots with various electrodes. All R_{total} *vs.* ($V_{bg} - V_{Dirac}$) curves show the asymmetry in hole and electron transportation regions. R_{odd} is positive for Ag, Ti, Au, Pd–graphene devices, and negative for Al/SLG FETs.
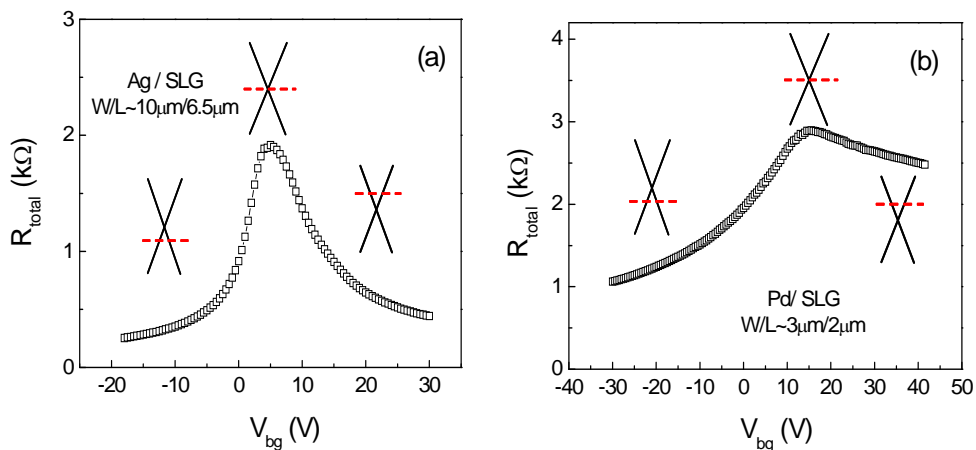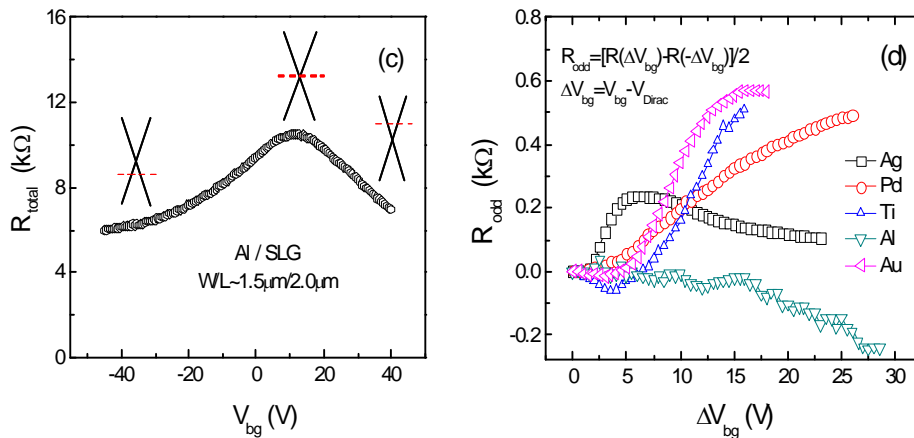
Figure 7. *Cont.*


4. Annealing Effect on Contact Junction

In order to improve the performance of graphene–metal contact, the forming gas annealing (FGA) were performed to examine the R_c of the sputtered Ti/SLG junction. Figure 8a shows the transfer characteristics of a SLG field-effect transistor before and after forming gas annealing (FGA), whereby the process is undergoing with N_2:H_2 mixing at 425 °C for half hours. After FGA treatment, the R_c could not be reduced as expected. The Raman spectra of the Ti/SLG contact are shown in Figure 8b. From Figure 8b, it is observed that the presence of the D band during the sputter process does not disappear, but rather expands. Concurrently, the FWHM of the G band also expands with the D band. The broadening of the D peak is correlated to the distribution of cluster with different orders and dimensions [58], thus suggesting that there are C–H sp^3 bonds [59] or carbon defects in the graphene layer underneath the metal after FGA treatment, which is very similar to amorphous carbon [58]. From Figure 8a again, it is interesting to observe that the Dirac point is shifted to the right direction, or positive polarity. The right shift of V_{Dirac}, and the ΔV_{Dirac} is more than 50 V, indicating a strong hole doping effect after FGA. The doped charge density, which is induced by FGA treatment, can be estimated by the following equation [60,61],

$$n = \frac{C_0 \Delta V_{Dirac}}{q} \tag{5}$$

where C_0 is the capacitance between channel and back-gate per unit area; ΔV_{Dirac} is the change in the voltage at the Dirac point, and q is the unit charge. For a 90-nm-thick SiO_2, $C_0 = \varepsilon_0 \varepsilon / d = 38.3$ nF/cm^2, where ε_0, ε is the permeability of vacuum and relative permittivity of the gate dielectric (3.9 for SiO_2), respectively. Accordingly, the FGA treatment-induced hole concentration is around $\sim 1 \times 10^{13}$ cm^{-2}. To further confirm this, Raman measurement in graphene channel is performed, as well. The absence of the D band in the channel also infers that the D band only stems from the high energetic sputter metal in our sputter sample. It was found that the G band had a right shift and the decrease is observed in its FWHM. The hole doping can be reflected in the stiffening and sharpening of the G band [39,62], as shown in Figure 8c. Raman examination of the blue shift reveals a decrease in full width at half maximum (FWHM) in the G band on the SLG channel, which indicates that the hole doping increases after FGA, leading to the Dirac point shifting toward high positive voltage [63]. A low temperature

rapid thermal annealing (RTA) is proposed to eliminate process-induced resistance [64], while RTA at high temperature will degrade the performance of the device.

Figure 8. (**a**) R_{total} of sputtered Ti/SLG device as a function of V_{bg} before and after forming gas annealing (FGA). The FGA does not improve R_c of Ti/SLG; (**b**) Raman spectra of Ti/SLG junction before and after FGA, the D band does not disappear; (**c**) Raman spectra of the graphene device channel before and after FGA.
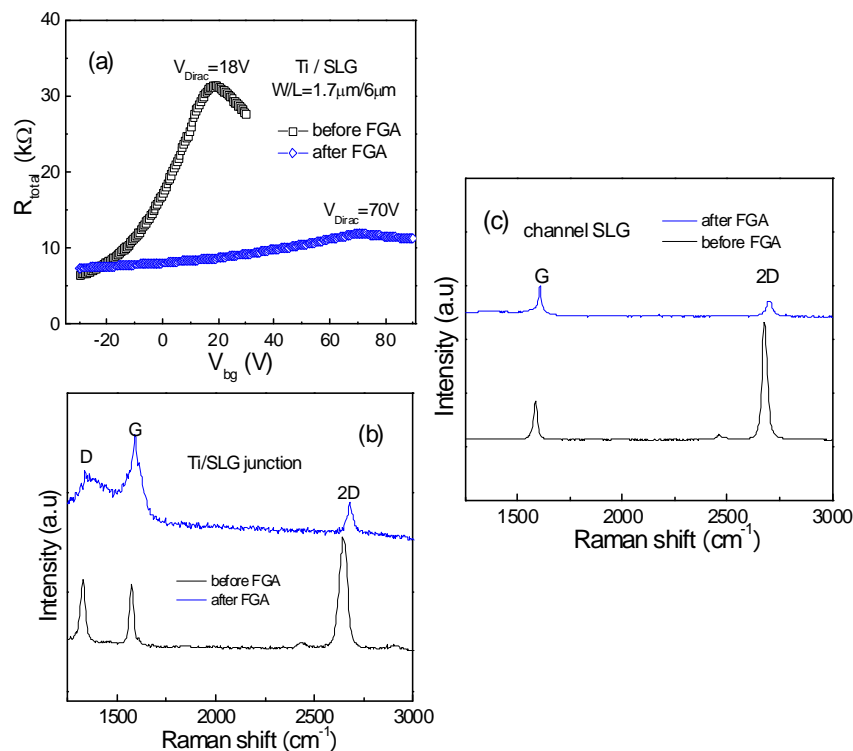

5. Interface Impact

There are two interfaces in a graphene–metal contact system: graphen/subtrate and graphene/metal interfaces. Graphene always physically lies on the surface of SiO_2/Si substrate, or another oxide/Si substrate, thus the first interface must necessarily be taken into account. Previously, the properties of graphene between SiO_2, Al_2O_3, and HfO_2 are studied by using Raman and atomic force microscopy (AFM) [65]. In addition to strong adhesion between graphene and dielectric, a higher hole concentration also occurs as graphene lies in a higher dielectric constant oxide. Figure 9a,b present the schematics illustration of SiO_2 surface treated by HF dipping and the re-oxidation process, respectively [66]. The difference between HF dipping and the re-oxidation process is that the SiO_2 surface is terminated by OH bonds for the former, and the latter is an O-terminated SiO_2 surface. The former is hydrophilic and dopes graphene into the p-type, while the latter is hydrophobic and dopes graphene into the n-type, which is verified in the Raman G band position [66,67]. It is also reported by Casiraghi *et al.* [68] that the G band position on substrates are within the range of fluctuation (1580–1588 cm^{-1}) by unintentional electron or hole doping effect for more than 40 graphene samples on SiO_2/Si substrate. Watanabe's observation shows that R_c is independent of work function of contact metal such as Ti, Ag, Co, Cr, Fe, Ni, and Pd [22]. Robinson *et al.* [69] also examined the effect of

work function difference on ρ_c with Al, Ti, Cu, Pd, Ni, Pt, where the work function difference with graphene varies from −0.2 eV to 1.2 eV. There is little difference in ρ_c as the difference in metal/graphene work function varies, indicating that the device fabrication process heavily influences one's ability to "dope" graphene [69]. This is the possible reason for contact resistance results widely varying among reported experiments, even for the same metal.

Figure 9. The schematics illustration of SiO_2 surface treated by (**a**) HP dipping; and (**b**) re-oxidation process. After HF solution dipping, the SiO_2 surface will mainly be terminated by OH bonds and some hydrocarbons (e.g., $-CH_3$). While for the reoxidation-treated sample, it is an O-terminated SiO_2 surface.
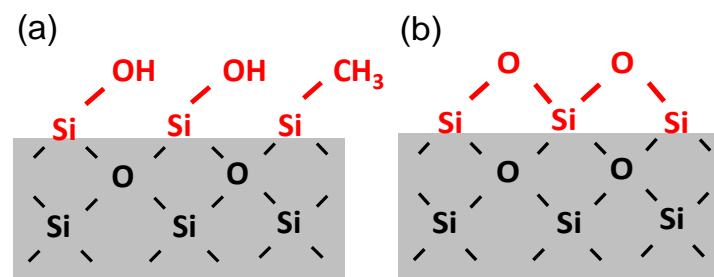
The second interface is also important for understanding graphene–metal contacts. Antonio *et al.* [70] ascribed double dip in $I_{ds} - V_{bg}$ to charge transfer between the graphene and the metal electrodes. Nouchi *et al.* [71] have also reported that anomalously distorted transportation originated from the partially formed oxide layer in Ni/graphene contact. The previous work assumed that carrier density of graphene underneath metal, described as segment 1 [52], is pinned [51,52,55]. It is independent from back-gate voltage, which was believed to modulate the graphene channel, rather than the graphene underneath metal. However, Raman and transfer measurements show that carrier density of graphene underneath metal can be modulated, indicating graphene contacting metal is still graphene because of a weak interaction [72]. In their experiments, there exists residual photo-resistor between (PR) graphene and metal. Chen [73], Xia [22] and Song's [74] observations also demonstrated that contact resistance is V_{bg} dependent, and also quantum capacitance is observed [74]. To eliminate the side effect of residual PR, Hsu *et al.* [75] intentionally inserted an Al sacrificial layer during lithography. Graphene surface roughness underneath the ohmic contacts is reduced; they were able to achieve the improved contact resistance to 200–500 Ω μm. Very recently, Nagashio *et al.* [76] developed a photo-resistor-free method to fabricate graphene FETs with Ni electrode. The modulation of the G band of Ni/graphene contact with and without residual PR is compared. The position of G band, corresponding to the doping effect, can be modulated up to 5 cm^{-1} for Ni/graphene with residual PR, while the shift of the G band is limited to 1–2 cm^{-1} in PR-free samples. It indicates that the graphene underneath metal even without residual PR is still graphene, but the modulation is restricted, due to strong interaction from $\pi - d$ coupling between graphene and Ni [50,77]. In the case of Ni/graphene with PR-free process, R_c is not improved compared to the case of PR. Theoretical calculation by Matsuda *et al.* [78] shows R_c will reduce in an "end-contacted" graphene–metal interface, where carbon $p\pi$ orbitals, as well as $p\sigma$ orbitals, play important roles in cohesion. Therefore, a sandwich contact structure (metal–graphene–metal) [79,80] and graphitic contact [76] has been suggested to reduce R_c.

6. Conclusions

We discuss the characteristics of graphene-metal contact from the viewpoints of metal preparation, asymmetric transportation, annealing effect, and interface impact. These findings provide insightful information into process optimization not only for graphene devices, but also for other layer-material devices such as MoS_2, WS_2.

Acknowledgments

Conflict of Interest

The authors declare no conflict of interest.

References

1. Novoselov, K.S.; Geim, A.K.; Morozov, S.V.; Jiang, D.; Zhang, Y.; Dubonos, S.V.; Grigorieva, I.V.; Firsov, A.A. Electric field effect in atomically thin carbon films. *Science* **2004**, *306*, 666–669.
2. Zhang, Y.; Tan, Y.W.; Stormer, H.L.; Kim, P. Experimental observation of the quantum hall effect and Berry's phase in graphene. *Nature* **2005**, *438*, 201–204.
3. Geim, A.K.; Novoselov, K.S. The rise of graphene. *Nat. Mater.* **2007**, *6*, 183–191.
4. Chen, Z.; Lin, Y.M.; Rooks, M.J.; Avouris, Ph. Graphene nano-ribbon electronics. *Phys. E* **2007**, *40*, 228–232.
5. Schedin, F.; Geim, A.; Morozov, S.V.; Hill, E.W.; Blake, P.; Katsnelson, M.I.; Novoselov, K.S. Detection of individual gas molecules adsorbed on graphene. *Nat. Mater.* **2007**, *6*, 652–655.
6. Lemme, M.C.; Echtermeyer, T.J.; Baus, M.; Kurz, H. A graphene field-effect device. *IEEE Electron. Dev. Lett.* **2007**, *28*, 282–284.
7. Murali, R.; Yang, Y.X.; Brenner, K.; Beck, T.; James, D.M. Breakdown current density of graphene nanoribbons. *Appl. Phys. Lett.* **2009**, *94*, 243114:1–243114:3.
8. Li, X.; Wang, X.; Zhang, L.; Lee, S.; Dai, H. Chemically derived, ultrasmooth graphene nanoribbon semiconductors. *Science* **2008**, *319*, 1229–1232.
9. Castro Neto, A.H.; Guinea, F.; Peres, N.M.R.; Novoselov, K.S.; Geim, A.K. The electronic properties of graphene. The electronic properties of graphene. *Rev. Mod. Phys.* **2009**, *81*, 109–162.
10. Lin, Y.M.; Dimitrakopoulos, C.; Jenkins, K.A.; Farmer, D.B.; Chiu, H.Y.; Grill, A.; Avouris, Ph. 100-GHz transistors from wafer-scale epitaxial graphene. *Science* **2010**, *327*, 662.
11. Schwierz, F. Graphene transistors. *Nat. Nanotechnol.* **2010**, *5*, 487–496.
12. Bolotin, K.I.; Sikes, K.J.; Jiang, Z.; Fundenberg, G.; Hone, J.; Kim, P.; Stormer, H.L. Ultrahigh electron mobility in suspended graphene. *Solid State Commun.* **2008**, *146*, 351–355.

13. Fan, X.Y.; Nouchi, R.; Yin, L.C.; Tanigaki, K. Effects of electron-transfer chemical modification on the electrical characteristics of graphene. *Nanotechnology* **2010**, *21*, 475208:1–475208:5.

14. Hong, S.K.; Kim, J.E.; Kim, S.O.; Choi, S.Y.; Cho, B.J. Flexible resistive switching memory device based on graphene oxide. *IEEE Electron. Dev. Lett.* **2010**, *31*, 1005–1007.

15. Jeong, H.Y.; Yun, J.; Kim, J.Y.; Hwang, J.O.; Kim, J.E.; Lee, J.Y.; Yoon, T.H.; Cho, B.J.; Kim, S.O.; Ruoff, R.S.; *et al*. Graphene oxide thin films for flexible nonvolatile memory applications. *Nano Lett.* **2010**, *10*, 4381–4386.

16. Eda, G.; Lin, Y.Y.; Miller, S.; Chen, C.W.; Su, W.F.; Chhowalla, M. Transparent and conducting electrodes for organic electronics from reduced graphene oxide. *Appl. Phys. Lett.* **2008**, *92*, 233305:1–233305:3.

17. Yan, X.; Cui, X.; Li, B.; Li, L.S. Large, solution-processable graphene quantum dots as light absorbers for photovoltaics. *Nano Lett.* **2010**, *10*, 1869–1873.

18. Nagashio, K.; Nishimura, T.; Kita, K.; Toriumi, A. Metal/Graphene Contact as a Performance Killer of Ultra-high Mobility Graphene—Analysis of Intrinsic Mobility and Contact Resistance. Presented at the International Electron Devices Meeting, Washington DC, USA, 7–9 December 2009.

19. Nagashio, K.; Nishimura, T.; Kita, K.; Toriumi, A. Contact resistivity and current flow path at metal/graphene contact. *Appl. Phys. Lett.* **2010**, *97*, 143514:1–143514:3.

20. Venugopal, A.; Colombo, L.; Vogel, E.M. Contact resistance in few and multilayer graphene devices. *Appl. Phys. Lett.* **2010**, *96*, 013512:1–013512:3.

21. Xia, F.; Perebeions, V.; Lin, Y.M.; Wu, Y.Q.; Avouris, Ph. The origins and limits of metal graphene junction resistance. *Nat. Nanotechnol*. **2011**, *6*, 179–184.

22. Watanabe, E.; Conwill, A.; Tsuya, D.; Koide, Y. Low contact resistance metals for graphene based devices. *Diam. Relat. Mater*. **2012**, *24*, 171–174.

23. Huard, B.; Stander, N.; Sulpizio, J.A.; Goldhber-Gordon, D. Evidence of the role of contacts on the observed electron-hole asymmetry in graphene. *Phys. Rev. B* **2008**, *78*, 121402:1–121402:4.

24. Liu, W.; Li, M.; Xu, S.; Zhang, Q.; Pey, K.L.; Hu, H.; Shen, Z.; Zou, X.; Wang, J.; Wei, J.; *et al*. Understanding the Contact Characteristics in Single or Multi-Layer Graphene Devices: The Impact of Defects (Carbon Vacancies) and the Asymmetric Transportation Behavior. Presented at the International Electron Devices Meeting, San Francisco, CA, USA, 6–8 December 2010.

25. Dai, H. Carbon nanotubes: Opportunities and challenges. *Surf. Sci*. **2002**, *500*, 218–241.

26. Blake, P.; Yanga, R.; Morozova, S.V.; Schedin, F.; Ponomarenkoa, L.A.; Zhukova, A.A.; Nair, R.R.; Grigorieva, I.V.; Novoselov, K.S.; Geim, A.K. Influence of metal contacts and charge inhomogeneity on transport properties of graphene near the neutrality point. *Solid State Commun*. **2009**, *149*, 1068–1071.

27. Liu, W.J.; Yu, H.Y.; Wei, J.; Li, M.F. Impact of process induced defects on the contact characteristics of ti/graphene devices. *Electrochem. Solid State Lett.* **2011**, *14*, K67–K69.

28. Magna, L.; Deretzis, I. Theoretical study of the role of metallic contacts in probing transport features of pure and defected graphene nanoribbons. *Nanoscale. Res. Lett*. **2011**, *6*, 234:1–234:5.

29. Seol, G.; Guo, J. Metal contact to graphene nanoribbon. *Appl. Phy. Lett.* **2012**, *100*, 063108:1–063108:4.

30. Russo, S.; Craciun, M.F.; Yamamoto, M.; Morpurgo, A.F.; Tarucha, S. Contact resistance in graphene-based devices. *Physica E* **2010**, *42*, 677–679.

31. Pimenta, M.A.; Dresselhaus, G.; Dresselhaus, M.S.; Cancado, L.G.; Jorioa, A.; Saitoe, R. Studying disorder in graphite-based systems by Raman spectroscopy. *Phys. Chem. Chem. Phys.* **2007**, *9*, 1276–1291.

32. Ferrari, A.C.; Meyer, J.C.; Scardaci, V.; Casiraghi, C.; Lazzeri, M.; Mauri, F.; Piscanec, S.; Jiang, D.; Novoselov, K.S.; Roth, S.; *et al*. Raman spectrum of graphene and graphene layers. *Phys. Rev. Lett.* **2006**, *97*, 187401:1–187401:4.

33. Ni, Z.H.; Wang, H.M.; Kasim, J.; Fan, H.M.; Yu, T.; Wu, Y.H.; Peng, Y.P.; Shen, Z.X. Graphene thickness determination using reflection and contrast spectroscopy. *Nano Lett.* **2007**, *7*, 2758–2763.

34. Wang, Y.Y.; Ni, Z.H.; Yu, T.; Shen, Z.X.; Wang, H.M.; Wu, Y.H.; Chen, W.; Wee, A. Raman studies of monolayer graphene: The substrate effect. *J. Phys. Chem. C* **2008**, *112*, 10637–10640.

35. Ni, Z.H.; Wang, H.M.; Ma, Y.; Kasim, J.; Wu, Y.H.; Shen, Z.X. tunable stress and controlled thickness modification in graphene by annealing. *ACS Nano* **2008**, *2*, 1033–1039.

36. Liu, W.; Tran, X.; Liu, X.; Wei, J.; Yu, H.; Sun, X. Characteristics of a single-layer graphene field effect transistor with UV/Ozone treatment. *Electrochem. Solid State Lett.* **2013**, *2*, M1–M4.

37. Xu, C.H.; Fu, C.L.; Pedraza, D.F. Simulation of point-defect properties in graphite by a tight-binding-force model. *Phys. Rev. B* **1993**, *48*, 13273–13279.

38. El-Barbary, A.; Telling, R.H.; Ewels, C.P.; Heggie, M.I.; Briddon, P.R. Structure and energetics of the vacancy in graphite. *Phys. Rev. B* **2003**, *68*, 144107:1–144107:7.

39. Yan, J.; Zhang, Y.B.; Kim, P.; Pinczuk, A. Electric field effect tuning of electron-phonon coupling in graphene. *Phys. Rev. Lett.* **2007**, *98*, 166802:1–166802:4.

40. Ni, Z.; Yu, T.; Luo, Z.; Wang, Y.; Liu, L.; Wong, C.; Miao, J.; Huang, W.; Shen, Z. Probing charged impurities in suspended graphene using raman spectroscopy. *ACS Nano* **2009**, *3*, 569–574.

41. Mohiuddin, T.M.G.; Lombardo, A.; Nair, R.R.; Bonetti, A.; Savini, G.; Jalil, R.; Bonini, N.; Basko, D.M.; Gailiotis, C.; Marzari, N.; *et al*. Uniaxial strain in graphene by Raman spectroscopy: G peak splitting, Grüneisen parameters, and sample orientation. *Phy. Rev. B* **2009**, *79*, 205433:1–205433:8.

42. Ni, Z.H.; Yu, T.; Lu, Y.H.; Wang, Y.Y.; Feng, Y.P.; Shen, Z.X. Uniaxial strain on graphene: Raman spectroscopy study and band-gap opening. *ACS Nano* **2008**, *2*, 2301–2305.

43. Chen, J.H.; Cullen, W.G.; Jang, C.; Fuhrer, M.S.; Williams, E.D. Defect scattering in graphene. *Phys. Rev. Lett.* **2009**, *102*, 236805:1–236805:4.

44. Ni, Z.H.; Ponomarenko, L.A.; Nair, R.R.; Yang, R.; Anissimova, S.; Grigorieva, I.V.; Schedin, F.; Blake, P.; Shen, Z.X.; Hill, E.H.; *et al*. On resonant scatterers as a factor limiting carrier mobility in graphene. *Nano Lett.* **2010**, *10*, 3868–3872.

45. Lahiri, J.; Batzilla, M. Graphene destruction by metal-carbide formation: An approach for patterning of metal-supported graphene. *Appl. Phys. Lett.* **2010**, *97*, 023102:1–023102:3.

46. Li, H.; Zhang, Q.; Liu, C.; Xu, S.H.; Gao, P.Q. Ambipolar to unipolar conversion in graphene field-effect transistors. *ACS Nano* **2011**, *5*, 3198–3203.

47. Nagashio, K.; Toriumi, A. Density-of-states limited contact resistance in graphene field-effect transistors. *Jpn. J. Appl. Phys.* **2011**, *50*, 070108:1–070108:6.

48. Berdebes, D.; Low, T.; Sui, Y.; Appenzeller, J.; Lundstrom, M.S. Substrate gating of contact resistance in graphene transistors. *IEEE Trans. Electron. Dev.* **2011**, *58*, 3925–3932.

49. Giovannetti, G.; Khomyakov, P.A.; Brocks, G.; Karpan, V.M.; Brink, J.; Kelly, P.J. Doping graphene with metal contacts. *Phys. Rev. Lett.* **2008**, *101*, 026803:1–026803:4.

50. Khomyakov, P.A.; Giovannetti, G.; Rusu, P.C.; Brocks, G.; Brink, J.; Kelly, P.J. First-Principles study of the interaction and charge transfer between graphene and metals. *Phys. Rev. B* **2009**, *79*, 195425:1–195425:12.

51. Mueller, T.; Xia, F.; Freitag, M.; Tsang, J.; Avouris, Ph. Role of contacts in graphene transistors: A scanning photocurrent study. *Phys. Rev. B* **2009**, *79*, 245430:1–245430:6.

52. Xia, F.; Mueller, T.; Golizadeh-Mojarad, R.; Freitag, M.; Lin, Y.M.; Tsang, J.; Perebeinos, V.; Avouris, Ph. Photocurrent imaging and efficient photon detection in a graphene transistor. *Nano Lett.* **2009**, *9*, 1039–1044.

53. Lee, E.J.H.; Balasubramanian, K.; Weitz, R.; Burghard, M.; Kern, K. Contact and edge effects in graphene devices. *Nat. Nanotech.* **2008**, *3*, 486–490.

54. Farmer, D.B.; Golizadeh-Mojarad, R.; Perebeinos, V.; Lin, Y.M.; Tulevski, G.S.; Tsang, J.C.; Avouris, Ph. Chemical doping and electron-hole conduction asymmetry in graphene devices. *Nano Lett.* **2009**, *9*, 388–392.

55. Liu, W.J.; Yu, H.Y.; Xu, S.H.; Zhang, Q.; Zou, X.; Wang, J.L.; Pey, K.L.; Wei, J.; Zhu, H.L.; Li, M.F. Understanding asymmetric transportation behavior in graphene devices using scanning kelvin probe microscopy. *IEEE Electron. Dev. Lett.* **2011**, *32*, 128–131.

56. Wang, F.; Zhang, Y.; Tian, C.; Girit, C.; Zettl. A.; Crommie, M.; Shen, Y.R. Gate-variable optical transitions in graphene. *Science* **2008**, *320*, 206–209.

57. Zhao, P.; Zhang, Q.; Jena, D.; Koswatta, S.O. Influence of metal-graphene contact on the operation and scalability of graphene field-effect transistors. *IEEE Trans. Electron. Dev.* **2011**, *58*, 3170–3178.

58. Ferrari, A.C.; Robertson, J. Interpretation of Raman spectra of disordered and amorphous carbon. *Phys. Rev. B* **2000**, *61*, 14095–14107.

59. Elias, D.C.; Nair, R.R.; Moiuddin, T.M.G.; Morozov, S.V.; Blake, P.; Phalsall, M.; Ferrari, A.C.; Boukhvalov, D.W.; Kastsnelson, M.I.; Geim, A.K.; *et al.* Control of graphene's properties by reversible hydrogenation: Evidence for graphane. *Science* **2009**, *323*, 610–613.

60. Ni, Z.H.; Wang, M.H.; Luo, Z.Q.; Wang, Y.Y.; Yu, T.; Wu, Y.H.; Shen, Z.X. The effect of vacuum annealing on graphene. *J. Raman Spectrosc.* **2010**, *41*, 479–483.

61. Liu, W.J.; Sun, X.W.; Fang, Z.; Wang, Z.R.; Tran, X.A.; Wang, F.; Wu, L.; Ng, G.I.; Zhang, J.F.; Wei, J.; *et al.* Positive bias-induced Vth instability in single layer graphene field transistors. *IEEE Electron. Dev. Lett.* **2012**, *33*, 339–341.

62. Pisana, S.; Lazzeri, M.; Casiraghi, C.; Novoselov, K.S.; Geim, A.K.; Ferrari, A.C.; Mauri, F. Breakdown of the adiabatic Born-Oppenheimer approximation in graphene. *Nat. Mater.* **2007**, *6*, 198–201.

63. Liu, W.J.; Sun, X.W.; Tran, X.A.; Fang, Z.; Wang, Z.R.; Wang, F.; Wu, L.; Zhang, J.F.; Wei, J.; Zhu, H.L.; *et al.* Vth shift in single layer graphene field effect transistors and its correlation with raman inspection. *IEEE Trans. Dev. Mater. Reliab.* **2012**, *12*, 478–481.

64. Balci, O.; Kocabas, C. Rapid thermal annealing of graphene-metal contact. *Appl. Phys. Lett*. **2012**, *101*, 243105:1–243105:5.

65. Song, S.M.; Cho, B.J. Investigation of interaction between graphene and dielectrics. *Nanotechnology* **2010**, *21*, 335706:1–335706:6.

66. Nagashio, K.; Yamashita, T.; Fujita, J.; Nishimura, T.; Kita, K.; Toriumi, A. Impacts of Graphene/SiO$_2$ Interaction on FET Mobility and Raman Spectra in Mechanically Exfoliated Graphene Films. Presented at the International Electron Devices Meeting, San Francisco, CA, USA, 6–8 December 2010.

67. Nagashio, K.; Yamashita, T.; Fujita, J.; Nishimura, T.; Kita, K.; Toriumi, A. Electrical transport properties of graphene on SiO$_2$ with specific surface structures. *J. Appl. Phys*. **2011**, *110*, 024513:1–024513:6.

68. Casiraghi, C.; Pisana, S.; Novoselov, K.S.; Geim, A.K.; Ferrari, A.C. Raman fingerprint of charged impurities in graphene. *Appl. Phys. Lett*. **2007**, *91*, 233108:1–233108:3.

69. Robinson, J.A.; Bella, M.; Zhu, M.; Hollander, M.; Kasarda, R.; Hughes, Z.; Trumbull, K.; Cavalero, K.; Snyder, D. Contacting graphene. *Appl. Phys. Lett*. **2011**, *98*, 053103:1–053103:3.

70. Bartolomeo, A.; Giubileo, F.; Santandrea, S.; Romeo, F.; Citro, R.; Schroeder, T.; Lupina, G. Charge transfer and partial pinning at the contacts as the origin of a double dip in the transfer characteristics of graphene-based field-effect transistors. *Nanotechnology* **2011**, *22*, 275702:1–275702:8.

71. Nouchi, R.; Tanigaki, K. Charge-Density depinning at metal contacts of graphene field-effect transistors. *Appl. Phys. Lett*. **2010**, *96*, 253503:1–253503:3.

72. Nagashio, K.; Moriyama, T.; Ifuku, R.; Yamashita, T.; Nishimura, T.; Toriumi, A. Is Graphene Contacting with Metal Still Graphene? Presented at the International Electron Devices Meeting, Washington DC, USA, 5–7 December 2011.

73. Chen, Z.; Appenzeller, J. Gate Modulation of Graphene Contacts—On the Scaling of Graphene FETs. Presented at the Proceeding of VLSI Tech, Honolulu, Hawaii, HI, USA, 17–19 June 2008.

74. Song, S.M.; Park, J.K.; Sul, O.J.; Cho, B.J. Determination of work function of graphene under a metal electrode and its role in contact resistance. *Nano Lett*. **2012**, *12*, 3887–3892.

75. Hsu, A.; Wang, H.; Kim, K.K.; Kong, J.; Palacios, T. Impact of graphene interface quality on contact resistance and RF device performance. *IEEE Electron. Dev. Lett*. **2011**, *32*, 1008–1010.

76. Nagashio, K.; Ifuku, R.; Moriyama, T.; Yamashita, T.; Nishimura, T.; Toriumi, A. Intrinsic Graphene/Metal Contact. Presented at the International Electron Devices Meeting, San Francisco, CA, USA, 10–12 December 2012.

77. Oshimay, C.; Nagashimaz, A. Ultra-Thin epitaxial films of graphite and hexagonal boron nitride on solid surfaces. *J. Phys. Condens. Matter* **1997**, *9*, 1–20.

78. Matsuda, Y.; Deng, W.Q.; Goddard, W.A., III. Contact resistance for "End-Contacted" metal-graphene and metal-nanotube interfaces from quantum mechanics. *J. Phys. Chem. C* **2010**, *114*, 17845–17850.

79. Gong, C.; Hinojos, D.; Wang, W.C.; Nijem, N.; Shan, B.; Wallace, R.M.; Cho, K.; Chabal, Y.J. Metal-Graphene-Metal sandwich contacts for enhanced interface bonding and work function control. *ACS Nano* **2012**, *6*, 5381–5387.

80. Franklin, A.D.; Han, S.J.; Bol, A.A.; Perebeinos, V. Double contacts for improved performance of graphene transistors. *IEEE Electron. Dev. Lett*. **2012**, *33*, 17–19.